Aerosol Science and Technology

ISSN: 0278-6826 (Print) 1521-7388 (Online) Journal homepage: https://www.tandfonline.com/loi/uast20

Evolution of maturity levels of the particle surface and bulk during soot growth and oxidation in a flame

K. O. Johansson, F. El Gabaly, P. E. Schrader, M. F. Campbell & H. A. Michelsen

To cite this article: K. O. Johansson, F. El Gabaly, P. E. Schrader, M. F. Campbell & H. A. Michelsen (2017) Evolution of maturity levels of the particle surface and bulk during soot growth and oxidation in a flame, Aerosol Science and Technology, 51:12, 1333-1344, DOI: 10.1080/02786826.2017.1355047

To link to this article: https://doi.org/10.1080/02786826.2017.1355047

AEROSOL SCIENCE AND TECHNOLOGY
2017, VOL. 51, NO. 12, 1333–1344
https://doi.org/10.1080/02786826.2017.1355047

LASER-INDUCED INCANDESCENCE FOR PARTICLE MEASUREMENTS: KNOWLEDGE GAPS, MEASUREMENT ARTIFACTS, AND NEW APPROACHES

Evolution of maturity levels of the particle surface and bulk during soot growth and oxidation in a flame

K. O. Johansson[a], F. El Gabaly[b], P. E. Schrader[a], M. F. Campbell[a], and H. A. Michelsen[a]

[a]Combustion Research Facility, Sandia National Laboratories, Livermore, California, USA; [b]Materials Physics Department, Sandia National Laboratories, Livermore, California, USA

ABSTRACT

We performed a study of the evolution of soot composition and fine structure, i.e., maturity level, in an atmospheric ethylene-air diffusion flame. We used laser-induced incandescence (LII) to provide information about maturity level of the bulk primary particle and X-ray photoelectron spectroscopy (XPS) to provide complementary information about particle-surface-maturity level. The results demonstrate that the bulk material and the particle surface evolve separately in the flame. Increased soot-maturity level is associated with increased long-range order of the particle fine structure. This increased order leads to an increase in the absorption cross-section in the visible and near-infrared and a shift of the absorption to longer wavelengths with increasing maturity level of the bulk particle. These trends result in a decrease in the dispersion exponent (ξ) and increase in the absorption cross-section scaling factor (β), as inferred from LII measurements. LII measurements demonstrate that bulk-maturity level increases with height-above-the-burner (HAB) until it reaches a plateau in the center of the flame at the maximum in the soot volume fraction. Bulk-maturity level only slightly decreases as soot is oxidized at larger HABs. Increased maturity level also leads to an increase in long-range sp^2 hybridization. XPS measurements of the sp^2/defect ratio demonstrate an increase in soot surface-maturity level with increasing HAB, but the surface-maturity level increases more gradually with HAB than the bulk-maturity level. Whereas the bulk-fine-structure order decreases slightly in the oxidation region, the surface order decreases dramatically, indicating that oxidation occurs preferentially at the surface under these conditions.

ARTICLE HISTORY
Received 13 January 2017
Accepted 28 June 2017

EDITOR
Thomas Kirchstetter

1. Introduction

Despite decades of research, many of the fundamental concepts behind soot formation, physical evolution during combustion, and oxidation are uncertain. The first step in soot formation is hypothesized to occur through nucleation or chemical growth of polycyclic aromatic hydrocarbons (PAHs; Richter and Howard 2000; Wang 2011). Experimental evidence indicates that particles formed during soot inception are composed of either randomly ordered aromatic structures with some aliphatic content or stacked PAHs held together by van der Waals forces (Michelsen 2017). These incipient particles are thought to grow by coalescence and PAH condensation. As these particles evolve, they lose hydrogen and become more carbonaceous, forming so-called "primary particles" that agglomerate instead of coalescing. Continued dehydrogenation leads to primary particles with graphite-like fine structure, and continued surface growth transitions loosely bound agglomerates into covalently bound aggregates of primary particles held together, at least partially, by graphite over-layers. Incipient (i.e., freshly formed) soot particles are less than ~6 nm in size, have carbon-to-hydrogen (C/H) ratios in the range of 1.4–2.5, and may contain oxygen. Mature soot is composed of primary particles with diameters of 10–50 nm, C/H ratios in the range of 10–20, and turbostratic polycrystalline graphite-like fine structure; these primary particles are bound together into dendritic aggregates of varying size, typically on the order of hundreds of nanometers. Whereas mature soot strongly absorbs light over a broad spectral range from ultraviolet (UV) to infrared (IR), incipient particles tend to absorb

CONTACT H. A. Michelsen hamichelsen2@gmail.com Combustion Research Facility, Sandia National Laboratories, 7011 East Ave., Livermore, CA 94550, USA.

Color versions of one or more of the figures in the article can be found online at www.tandfonline.com/uast.

Supplemental data for this article can be accessed on the publisher's website.

more strongly at shorter (i.e., UV and visible) wavelengths (Michelsen 2017, and references therein).

Soot characteristics evolve continuously during combustion as the level of particle maturity increases, i.e., as particles transition from incipient particles composed of large disordered molecular structures with low C/H ratios and mixed *sp*, sp^2, and sp^3 carbon hybridization to graphite-like mature particles with high C/H ratios, predominantly sp^2-hybridized carbon, and more ordered fine structure. How these characteristics evolve, however, is poorly understood (DOE 2006). It may be expected, for instance, that the aromatic to aliphatic character should increase with increasing level of soot maturity, and some studies have experimentally demonstrated this behavior (Santamaria et al. 2006; Santamaria et al. 2010; Russo et al. 2015). Other studies, however, have appeared to show the reverse trend (McKinnon et al. 1996; Öktem et al. 2005; di Stasio et al. 2006; Cain et al. 2010). One reason for the poor understanding of the evolution of soot characteristics and the processes that control them is attributable to limitations in available measurement techniques. There is thus a strong need for diagnostics that can provide an assessment of particle-maturity level (Michelsen 2017). In addition, developing a detailed description of soot growth, graphitization, and oxidation will require techniques that can distinguish between surface and bulk properties of the particles. Mechanisms that contribute to particle growth, for instance, are expected to take place on the surface. Graphitization initiated by pyrolytic loss of hydrogen may take place throughout the particle bulk while graphitization initiated by oxidative defect generation may preferentially proceed at the particle surface.

Because the optical properties of soot change as particles evolve, there is a potential to exploit these changes for *in situ* optical measurements of soot-maturity level. In particular, the average magnitude of the absorption cross-section increases with increasing C/H ratio, increasing sp^2 hybridization, and generally increasing soot-maturity level (Foster and Howarth 1968; Batten 1985; Habib and Vervisch 1988; Minutolo et al. 1996; Hopkins et al. 2007; López-Yglesias et al. 2014); the absorption cross-section also exhibits a bathochromic shift (i.e., a shift to longer wavelengths) with increasing particle-maturity level (Millikan 1961; Siddall and McGrath 1963; Dalzell and Sarofim 1969; D'Alessio et al. 1972; Habib and Vervisch 1988; Minutolo et al. 1996; Cléon et al. 2011; Migliorini et al. 2011; López-Yglesias et al. 2014; Leschowski et al. 2015; Russo et al. 2015; Simonsson et al. 2015). Other work has attempted to characterize the wavelength dependence of the absorption cross-section on the organic carbon (OC) to total carbon (TC) content of soot emitted from flames (Schnaiter et al. 2006; Kim et al. 2015; Bescond et al. 2016). Although the flames and extraction methods were not well controlled for levels of soot maturity, these studies demonstrated a bathochromic shift with decreasing OC/TC ratio, which is consistent with the C/H-ratio trends discussed above and with atmospheric combustion emissions (Hopkins et al. 2007; Pokhrel et al. 2016). Most atmospheric studies of correlations of the dispersion (Ångström) exponent with the OC/TC ratio are focused on understanding the properties of soot particles with heavy hydrocarbon coatings often accumulated in exhaust plumes or during aging in the atmosphere and are not relevant to studies of soot evolution during combustion. Bescond et al. (2016) extended these studies to include amorphous carbon particles produced by an arc discharge between graphite rods in order to develop a model of particle properties ranging from amorphous to graphitic carbon. Considerable experimental evidence and computational work indicates, however, that incipient particles are composed of disordered large molecular species with sizes of ~1 nm and C/H ratios of ~2 (Richter and Howard 2000; Wang 2011; Michelsen 2017). Amorphous carbon generated by an arc discharge, on the other hand, has a mixture of sp^2 and sp^3 hybridized carbon with dangling bonds, C/H ratios >15, and minimal order on a nanometer scale (Wentzel et al. 2003; Su et al. 2005; Bescond et al. 2016). Although the model proposed by Bescond et al. (2016) is thus not directly applicable to our studies or to soot in particular, it is a valuable step toward a detailed description of properties of carbonaceous particles.

Extinction measurements performed *in situ* in flames at different wavelengths can provide information about the wavelength dependence of the absorption (D'Alessio et al. 1972; Minutolo et al. 1996; Migliorini et al. 2011; Leschowski et al. 2015; Simonsson et al. 2015). Because extinction is the result of the combination of absorption and scattering, this technique relies on assumptions about the scattering component in order to infer the wavelength dependence of the absorption. Scattering can be significant, however, and difficult to take into account. In addition, extinction is a path-integrated line-of-sight measurement, and both the scattering contribution and particle-maturity level can vary substantially along the measurement path, which can complicate the interpretation. Furthermore, interferences by gas-phase species absorption can also perturb extinction measurements (Migliorini et al. 2011; Yapp et al. 2016). Laser-induced incandescence (LII), on the other hand, is an *in situ* optical technique that is sensitive to soot absorption, is not path integrated (i.e., is not a line-of-sight technique), and can be used to infer information about soot-maturity level through measurements made at multiple laser wavelengths (Cléon et al. 2011; López-Yglesias et al. 2014; Migliorini et al. 2015). LII involves heating particles with a high-power laser and measuring the resulting quasi-blackbody emission (Michelsen et al. 2015). Although several studies have shown a correlation

between the dispersion exponent and the C/H ratio (Millikan 1961; Siddall and McGrath 1963; Dalzell and Sarofim 1969; D'Alessio et al. 1972; Habib and Vervisch 1988; Minutolo et al. 1996) and the percent sp^2 hybridization (Hopkins et al. 2007), there is still some uncertainty about its interpretation with respect to the level of soot maturity and the corresponding physical characteristics.

X-ray photoelectron spectroscopy (XPS) is an *ex situ* technique that is sensitive to the chemical environment of atoms in a sample, is quantitative, and provides a measure of atomic composition, surface functional groups, and electronic structure, including carbon hybridization (Müller et al. 2007; Jaramillo et al. 2014). XPS involves illuminating the sample with an X-ray beam to eject core electrons from atoms in the sample and measuring the kinetic energy of the electrons ejected. The difference in energy between the photon energy and the electron kinetic energy yields the binding energy of the electron. At the photon energy used in this study (1253.6 eV), the electron mean free path in graphite is on the order of 1–2 nm (Tanuma et al. 2011). XPS signal originating from a depth of ~1 nm is reduced by a factor $1/e$ relative to the surface, making XPS sensitive to only the surface layers of the particle. This surface sensitivity is a good complement to the bulk sensitivity of LII. Aerosol mass spectrometry (AMS) provides information about semi-volatile species that are condensed on or in the particle either in the flame or in our sampling probe and a measure of particle-precursor-species abundance. We have combined LII and XPS measurements on soot produced in a partially premixed atmospheric ethylene-air diffusion flame to gain insight into the evolution of soot bulk- and surface-maturity level during combustion. We have also used AMS to yield information about the availability of heavy hydrocarbons that can participate in particle growth.

2. Experimental approach

2.1. Burner

We used a newly designed burner to produce a laminar partially premixed diffusion flame with a visible flame height of ~11 mm. The burner is a hybrid of a conventional Hencken-type burner and a slot burner consisting of a row of small-gauge fuel tubes inserted into a hexmesh supplying air. Further details are given in Campbell et al. (2016). We used ethylene as the fuel with a flow rate of 0.2 standard liters/min (slm, referenced to 0°C and 101325 Pa) and air as the co-flow with a flow rate of 14.0 slm.

2.2. Laser-induced incandescence (LII) measurements

Details about the setup used for the LII measurements are given in Section S1.1 of the online supplemental information (SI). We recorded LII signals at different heights above the burner (HABs) over a wide range of laser fluences at laser wavelengths of 1064 and 532 nm. The laser beam was passed through the center of the flame collinear with the long axis of the burner. The detector was positioned perpendicular to the laser beam to collect signal from the center of the long axis of the flame. Each LII measurement was repeated three times and then averaged. Laser-beam attenuation during propagation through the flame to the measurement volume was obtained from extinction measurements and taken into account during LII-data evaluation by weighting the fluence at the laser output by the square root of the transmittance. Values for transmittance at 1064 and 532 nm at different HABs were taken from Campbell et al. (2016).

2.3. X-ray photoelectron spectroscopy (XPS) measurements

We performed XPS measurements over the O 1*s* peak near 532 eV and the C 1*s* peak near 284 eV on soot extracted at different HABs in the flame. The XPS measurements were performed using an Omicron DAR400 Mg K-alpha X-ray source and Physical Electronics 10–360 electron-energy analyzer. More details about the XPS measurements are given in Section S1.2 of the SI.

2.4. Aerosol mass spectrometry (AMS) measurements

We measured mass spectra of vaporized particles extracted at different HABs in the flame using a vacuum ultraviolet photoionization aerosol mass spectrometer (AMS). The AMS signal range spanned a mass range from ~90 to ~550 u, which corresponds to species containing ~7 to ~45 carbon atoms. Species detected using AMS had carbon-to-hydrogen (C/H) ratios less than 1 at the lowest masses and ≥~2.5 in the upper mass range. More details about these measurements are given in Section S1.3 of the SI.

3. Analysis approach

3.1. Inferring optical parameters from LII measurements

The primary particles in this flame have diameters that are less than 15 nm (Campbell et al. 2016). Because their

sizes are 50–100 times smaller than the laser wavelengths used for the LII measurements, the Rayleigh approximation is appropriate for these particles. The absorption cross-section, σ_{abs}, at wavelength λ of a spherical particle in the Rayleigh regime is expressed as

$$\sigma_{abs} = \frac{\pi^2 d^3}{\lambda} E(m,\lambda), \quad [1]$$

where d is the particle diameter, and $E(m, \lambda)$ is the dimensionless refractive-index function for absorption at a specific wavelength. We have no way of quantifying the thickness of the disordered surface layer and, for the sake of simplicity, assume that it is on the order of a monolayer or two and has little impact on the bulk optical properties. The absorption cross-section for soot particles deviates from the λ^{-1}-dependence of Equation (1), however, and this deviation in σ_{abs} evolves as the soot matures. The deviation from the λ^{-1}-dependence can be expressed by imposing a dispersive wavelength-dependence on $E(m, \lambda)$ (Michelsen 2003), i.e.,

$$E(m,\ \lambda) = \frac{\lambda^{1-\xi}\beta}{6\pi}, \quad [2]$$

where β (units of $cm^{\xi-1}$) is an empirical scaling factor that does not depend on wavelength but does increase with soot-maturity level and particle temperature. The dispersion exponent or Ångström exponent, ξ, also depends on soot-maturity level. As the absorption cross-section shifts to longer wavelengths with increasing maturity level, ξ decreases.

In pulsed LII using nanosecond laser pulses for particle heating, the rate of absorptive heating during the laser pulse exceeds other heating and cooling rates at atmospheric pressure if the laser fluence is lower than ~0.08 J/cm^2 at 532 nm or lower than ~0.15 J/cm^2 at 1064 nm (Michelsen et al. 2010). The laser-heating rate, however, depends on the absorption properties of the soot particles. The fluences required to heat identical particles under identical ambient conditions to the same temperature T_{max} using two different laser wavelengths depend linearly on the absorption cross-sections at these two wavelengths, which results in the relationship

$$\left[\frac{F(\lambda_1)}{F(\lambda_2)}\right]_{T_{max}} = \frac{\sigma_{abs}(\lambda_2)}{\sigma_{abs}(\lambda_1)}, \quad [3]$$

where $F(\lambda)$ is the excitation laser fluence at wavelength λ, and $\sigma_{abs}(\lambda)$ is the absorption cross-section at wavelength λ. In the current study, λ_1 is 1064 nm, and λ_2 is 532 nm, and the fluence ratio is determined by matching the LII signal, a proxy for temperature, as described below. Combining Equations (1), (2), and (3) and substituting S_{max} for T_{max} yields

$$\left[\frac{F(\lambda_1)}{F(\lambda_2)}\right]_{S_{max}} = \frac{\sigma_{abs}(\lambda_2)}{\sigma_{abs}(\lambda_1)} = \left(\frac{\lambda_1}{\lambda_2}\right)^{\xi}. \quad [4]$$

Solving Equation (4) for ξ gives the expression for the dispersion exponent, i.e.,

$$\xi = \frac{\ln\left[\frac{F(\lambda_1)}{F(\lambda_2)}\right]_{S_{max}}}{\ln\left(\frac{\lambda_1}{\lambda_2}\right)} = \frac{\ln\left[\frac{\sigma_{abs}(\lambda_2)}{\sigma_{abs}(\lambda_1)}\right]}{\ln\left(\frac{\lambda_1}{\lambda_2}\right)}. \quad [5]$$

The dispersion exponent ξ can thus be inferred by measuring the peak of the LII-temporal profile as a function of fluence at two laser wavelengths, as long as the laser wavelengths are long enough to avoid fluorescence and photodissociation of the particle. The wavelength dependence of the absorption cross-section is sometimes represented with respect to the ratio of $E(m, \lambda)$ at different wavelengths, which is related to ξ and the fluence ratio according to

$$\frac{E(m,\lambda_2)}{E(m,\lambda_1)} = \frac{\lambda_2}{\lambda_1}\left[\frac{F(\lambda_1)}{F(\lambda_2)}\right]_{S_{max}} = \left(\frac{\lambda_2}{\lambda_1}\right)^{1-\xi}. \quad [6]$$

A brief description on using the LII fluence curves to infer ξ and $E(m, \lambda_2)/E(m, \lambda_1)$ is given in Section S2.1 of the SI.

We have also used the normalized peak-LII signals to estimate the change in the magnitude of the absorption cross-section with HAB. The value of β is expected to increase with increasing soot-maturity level. We used the following relationship (derived in Section S2.2 of the SI) to estimate β using the peak-LII fluence curves:

$$\rho c_s (T_{max} - T_0)\lambda^{\xi} = \beta F(\lambda). \quad [7]$$

Here ρ is the primary-particle density; c_s is the specific heat; T_{max} is the particle temperature, and $F(\lambda)$ is the fluence, associated with the normalized peak-LII signal. The ambient temperature for each HAB in the flame T_0 is provided by Campbell et al. (2016). The peak-LII signal can be used as a proxy for maximum particle temperature for a particular laser fluence (Bambha et al. 2013). The method for estimating T_{max} based on S_{max} is given in Section S2.2 of the SI. We could have inferred temperatures using time-resolved incandescence measurements at two or more detection wavelengths, along with the inferred values for ξ as input for the wavelength dependence in the fit, but the calculated temperatures are sufficiently accurate to derive trends in β.

By plotting the left-hand side of the equation as a function of $F(\lambda)$ and performing a linear fit to the data, we can infer β from the slope of the line. Although this analysis will produce values of β with some uncertainty associated with neglecting the influence of other heat-transfer terms on the peak-LII signal, the trends in β should be sufficiently reliable to observe trends in soot-maturity levels.

Performing this analysis provides information about trends in β with soot-maturity level if the product ρc_s is independent of temperature and soot-maturity level. Section S2.2 of the SI demonstrates that the product ρc_s for graphite is nearly constant with temperature at a value of 4.59 ± 0.07 J/cm^{3}K over the temperature range of 1800–4000 K. The SI also provides a derivation for the product ρc_s for soot of varying levels of maturity, which is given by

$$\rho c_s = \frac{3R}{0.260884 a^2 c}, \qquad [8]$$

where R is the universal gas constant (8.3145 J/mol K), a is the length of the graphite unit cell in the basal plane in Ångströms (2.46 Å), and c is the interlayer spacing in Ångströms (3.36 Å for graphite at room temperature, 3.53 Å for graphite at 2000 K, 3.5 Å for soot; Spence 1963). Equation (8) yields a value of 4.51 J/cm^{3}K for ρc_s for soot of varying levels of maturity at high temperatures, which is consistent with the mean value for graphite. The density of soot is estimated to vary with level of maturity according to

$$\rho = \left(0.260884 a^2 c\right)^{-1} \left(\frac{w_C \frac{C}{H} + w_H}{\frac{C}{H} + 1} \right), \qquad [9]$$

where w_C is the molecular weight of carbon (12.011 g/mole), and w_H is the molecular weight of hydrogen (1.008 g/mole). Equation (9) yields reasonable room temperature values of 2.08 g/cm^3 for mature soot with a C/H ratio of 20 and 1.51 g/cm^3 for incipient soot with a C/H ratio of 2.

3.2. Inferring surface structure and composition from XPS measurements

We fit the XPS spectra following the outline presented by Smith et al. (2016), which yields internal consistency between the fits of the O 1*s* and C 1*s* signals. The peaks used in the fit are described in Section S2.3 and summarized in Tables S1 and S2 in the SI, where more detail about the fitting is provided. We used three of the peaks assigned in the C 1*s* fits to obtain a measure of trends in soot-surface-maturity level. We assume that, as the soot surface matures, the shape of the XPS C 1*s* spectrum becomes increasingly similar to the shape of the signal from highly ordered graphite. We measured the spectrum of highly ordered pyrolytic graphite (HOPG) as a calibration for the peak shape attributable to graphitic sp^2-hybridized carbon atoms. The spectral feature associated with graphitic sp^2-hybridized carbon atoms is sharp, asymmetric, and well defined. The C 1*s* electrons of other C-C and C-H sp^2-hybridized carbon atoms may have similar binding energies, but the shape of the features is broader and more symmetric. Our fitting of sp^2 features was more selective for graphitic sp^2-hybridized carbon atoms. The second and third peaks used to assess soot-surface-maturity level were denoted defect peaks. They were assigned symmetric curve shapes and were positioned on either side of the asymmetric sp^2 peak. The two defect peaks accounted for non-conjugated carbon atoms and carbon atoms in positions lacking a long-range sp^2-hybridized network. We expect aliphatic and small aromatic hydrocarbons, which do not demonstrate long-range graphitic sp^2 character, to add to the defect peaks, even though they may also yield some contributions to the graphitic sp^2 peak. We calculated the ratio between the area of the graphitic sp^2 peak and the sum of the areas of the defect peaks. Whereas aliphatic and small aromatic hydrocarbons yield low sp^2/defect ratios, perfect single-crystal graphite contains exclusively graphitic sp^2-hybridized carbon, which results in an infinitely high sp^2/defect ratio. Thus, we expect a particle consisting of condensed aromatic species to have a small sp^2/defect ratio that increases as the long-range graphitic order increases with increasing soot-surface-maturity level.

4. Results and discussion

4.1. Trends in bulk-maturity derived from LII measurements

Figure 1 shows the normalized peak-LII signals recorded at different HABs as a function of the laser fluence at 532 and 1064 nm. The maximum of each curve was normalized to unity. The peak-LII signal increases non-linearly with fluence at low and intermediate fluences. At high fluences, particles sublime, and the peak-LII signal reaches a plateau. When the particles sublime, the time-resolved LII-signal-decay rate increases sharply (Michelsen et al. 2015). As a result, the width of the peak in the temporal profile decreases with increasing fluence (Goulay et al. 2009, 2013). The sharpness of the peak at high fluence, coupled with the finite time resolution of the detection system, results in a small decrease in the peak signal with increasing fluence at high fluence.

Because the temporal profiles represent an average of 500 shots, small shot-to-shot time jitter on the trigger can also contribute to this effect (Goulay et al. 2009). A non-ideal homogenous spatial profile of the laser beam also enhances this effect. The effect is more pronounced at 532 nm because the absorption cross-section is larger for the shorter wavelength, and, at a particular fluence, the signal decay rates are faster, and the temporal peaks are sharper (Goulay et al. 2013).

At HABs below 4 mm, the fluence curves at 532 nm demonstrate significant interference from PAH laser-induced fluorescence (LIF) and are not shown in Figure 1. The 532 nm fluence curve at 4 mm also demonstrates a small amount of LIF interference. The shift of the fluence curves to lower fluences with increasing HAB indicates that the absorption cross-sections at both 532 and 1064 nm increase with increasing HAB throughout the flame. This behavior is consistent with previous observations (Cléon et al. 2011; Mouton et al. 2013; Bladh et al. 2015; Olofsson et al. 2015). Figure 1 also shows that the absorption cross-sections at 532 nm are higher than those at 1064 nm at all HABs, but the differences are more profound at low HABs than at high HABs.

We used the measurements shown in Figure 1 to derive ξ and β for each HAB between 4 and 9 mm, as described in Section 3.1; the results are presented in Figure 2a. The values of ξ shown in Figure 2a are averages for three different normalized signal levels (0.15, 0.25, and 0.35) that correspond to equivalent-temperature lines (e.g., Figure S4). The error bars represent the average standard deviation for these points. A description of the derivation of the error bars is provided in Section S2.4 in the SI. Figure 2a also shows values of β inferred from ξ via the maturity-level parameter X_{ann} using the parameterizations given by López-Yglesias et al. (2014), which attempted to account for soot-maturity level. Those parametrizations were derived based on LII-model comparisons with LII-temporal profiles from two other diffusion flames. The agreement between the values of β inferred from the parameterizations of López-Yglesias et al. (2014) and the values derived from the fluence curves in Figure 1 is demonstrated to be within 5%–19% at HABs between 5 and 7 mm and 2% at HABs $\geq$8 mm.

Over the range of HABs for which LII signal is measureable, the primary-particle size is in the range of 8–12 nm, as measured by transmission electron microscopy (TEM) and small-angle X-ray scattering (SAXS; Campbell et al., in preparation). Incipient particles composed of semi-volatile hydrocarbons are not expected to yield measureable LII signal because they tend not to absorb or emit strongly at visible and near-IR wavelengths and vaporize at relatively low

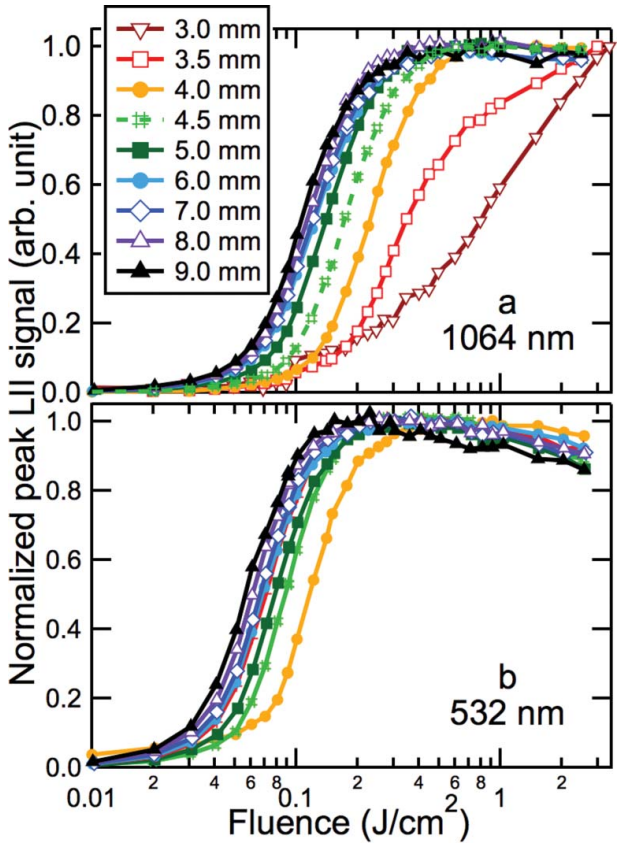

Figure 1. Normalized peak-LII signal as a function of laser fluence. Measurements were made at different HABs (see legend) at laser wavelengths of (a) 1064 nm and (b) 532 nm. Each curve was normalized to unity at the maximum value, and each point is an average of three measurements.

temperatures (Grotheer et al. 2011). Although we have measured particles at HABs below 4 mm using TEM and SAXS (Campbell et al., in preparation), these particles are not mature enough to produce significant LII signal. Thus, the LII signal depends on both the soot volume fraction and the level of soot maturity. Our volume-fraction measurements were calibrated relative to extinction at an HAB of 6 mm from mature-soot particles (see below) (Campbell et al. 2016) and are a proxy for the volume fraction of mature soot.

The value of ξ decreases, and the value of β increases dramatically at the lower HABs, demonstrating that the soot-bulk-maturity level increases rapidly with HAB at low HABs. The increase in soot-bulk-maturity level is approximately correlated with the mature-soot volume fraction, as measured by LII and shown in Figure 2b. The values of ξ and β are independent of HAB between 5 and 7 mm, demonstrating that the bulk-maturity level is constant in the region where the soot volume fraction is almost constant. Above 7 mm, oxidation leads to a slight decrease in the bulk-maturity level and a

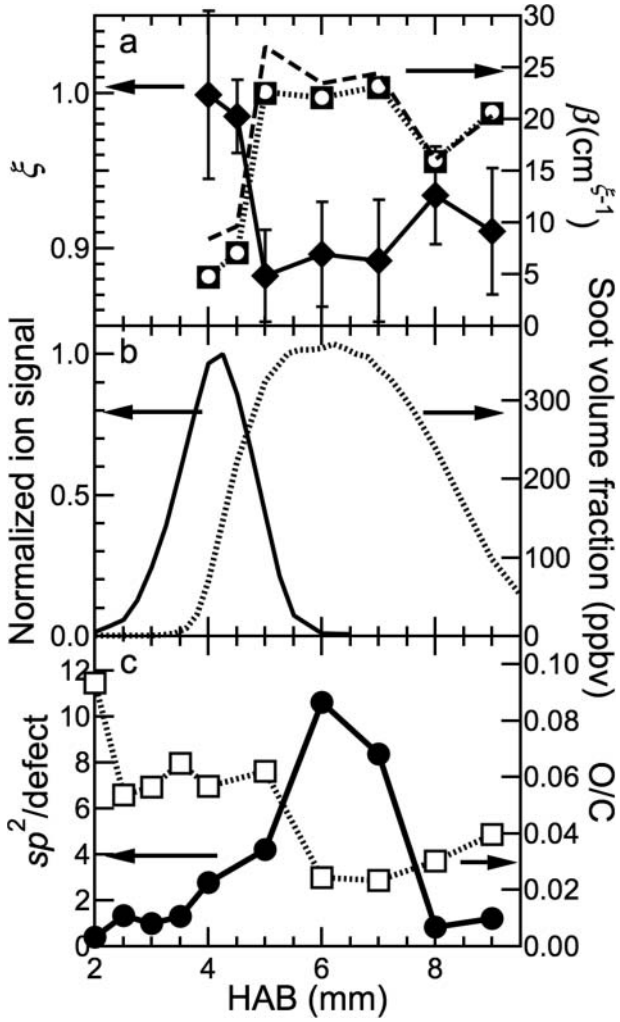

Figure 2. Optical properties derived from LII measurements, mature-soot volume fraction, normalized heavy hydrocarbon distribution, and XPS C 1*s* sp^2/defect and O/C ratios. Results are shown as a function of HAB for (a) the dispersion exponent (ξ) (diamonds relative to left axis), absorption cross-section scaling factor (β) (circles, squares, dashed, and dotted lines relative to right axis), (b) normalized AMS ion signal (line relative to left axis), mature-soot volume fraction (dotted line relative to right axis), (c) the ratio between the signal from sp^2-hybridized carbon atoms and carbon atoms in defect locations at the surface (circles relative to left axis), and the ratio of oxygen to carbon atoms at the surface (squares relative to right axis). In (a), β for 532 nm and 1064 nm are on top of each other; 1064 nm is represented as open circles, and 532 nm as solid squares. The dashed line represents β values inferred using the parameterizations given in López-Yglesias et al. (2014). In (b) the mature-soot volume-fraction measurements are from Campbell et al. (2016).

significant decrease in the volume fraction. The values of $E(m,532)/E(m,1064)$ corresponding to the values of ξ shown in Figure 2a span the range 0.92–1.00 in our flame (Figure S6 in the SI). These values are consistent with previous measurements in atmospheric premixed and diffusion flames, which span the range of 0.89–1.12 (Therssen et al. 2007; Michelsen et al. 2010; Yon et al. 2011; Michelsen et al. 2012; Bejaoui et al. 2014; López-Yglesias et al. 2014). All of these values are lower than the values of 1.35–1.95 reported by Cléon et al. (2011) for a low-pressure premixed flame.

4.2. Trends in surface-maturity level derived from XPS measurements

Figure 3 shows results of fits to XPS C 1*s* spectra at several HABs. Differences in the peak shapes and fits are observable at different HABs. For instance, the relative area of the sp^2 peak is significantly larger at 6 mm than

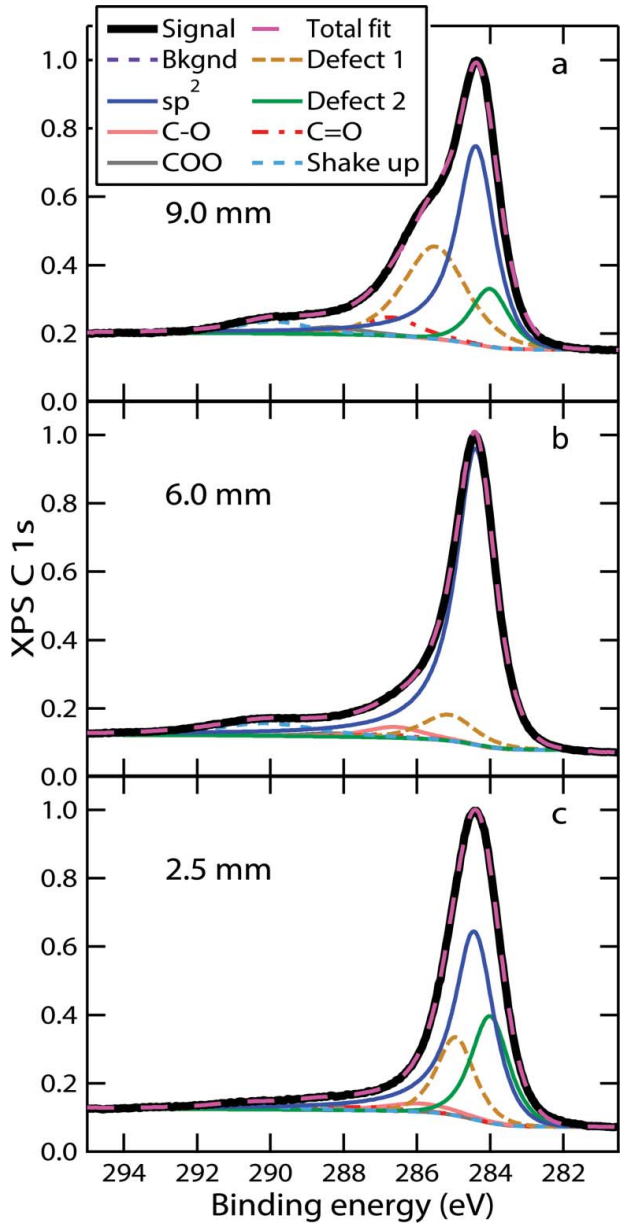

Figure 3. XPS C 1*s* spectra at selected HABs. Peaks used in the fit are given in Tables S1 and S2. The measured signal is indicated by the thick black line. The results of the fit are identified in the legend.

at 2.5 mm but smaller at 9 mm as defect and oxygenated peaks grow.

Figure 2c shows the ratio of sp^2-hybridized C atoms to C atoms in defect positions inferred from the fits to the XPS spectra. Figure 2c also shows the atomic oxygen to carbon ratio at the surface. The sp^2/defect ratio is low near the burner, and the O/C ratio is relatively high. These observations are consistent with incipient particles composed of condensed PAHs with some oxygen groups embedded in the particle (Johansson et al. 2016).

The sp^2/defect ratio increases with increasing HAB in the lower half of the flame, i.e., at HABs below ~6 mm; this result demonstrates that the surface-maturity level increases with increasing HAB and continues to increase with HAB well past the HAB of 5 mm, where the bulk-maturity level stops increasing, as shown by ξ and β in Figure 2a. The surface-maturity level increases gradually below an HAB of ~5 mm, while the O/C ratio is constant.

The reason for the slow growth in surface-maturity level, compared to the bulk-maturity level, may be attributable to high concentrations of PAHs and other large hydrocarbon species available to adsorb to, and react with, the soot surface (shown by the AMS ion signal in Figure 2b), continuously adding hydrogen-rich molecules to the surface. Strong AMS signal indicates coexistence of semi-volatile hydrocarbon species and particles larger than ~50 nm formed either in the flame or in the probe by gas-phase condensation on, or coagulation of, smaller particles. Particle growth by surface adsorption in the flame would require a relatively low hydrocarbon volatility, which is consistent with the onset of rapid growth and detection by LII at HABs above ~4 mm shown in Figure 2b. The decrease in AMS signal above ~5 mm HAB shows that the abundance of heavy hydrocarbon species is low at these HABs, making these species unavailable for participation in soot-particle surface growth.

The XPS results are consistent with soot growth via surface-addition reactions up to at least an HAB of 5 mm. Between 5 and 6 mm, the surface-maturity level increases more markedly than at lower HABs, suggesting much slower surface growth via hydrocarbon adsorption. This result is consistent with the lack of change in the soot-volume fraction in this region. This HAB range also corresponds to the region in the flame where the concentration of PAHs and other large gas-phase hydrocarbon species decrease to the baseline (Figure 2b) and are thus no longer available to contribute to additional surface growth. The O/C ratio also decreases substantially in this region.

At HABs above 6 mm, soot is in an oxidation region. The soot-volume fraction and the sp^2/defect ratio decrease somewhat between HABs of 6 and 7 mm, but ξ and β show negligible changes in this region, suggesting that the onset of oxidation leads to a reduction in the long-range order of the fine structure of the surface without affecting the bulk.

Between HABs of 7 and 8 mm, ξ increases, and β decreases, but these changes are small compared to the decrease in sp^2/defect ratio, which drops to values comparable to those of very immature soot particles found at HABs below 4 mm. Thus, the bond-hybridization scheme of C atoms changes dramatically at the surface, but the bulk material retains absorption characteristics that only deviate slightly from the absorption characteristics at ~6 mm HAB. The apparent small changes to the bulk-maturity level may be a reflection of the changes at the surface influencing the inferred values of ξ and β. The O/C ratio increases only slightly, which is consistent with most of the oxidation reaction leading to gas-phase species with volume-fraction loss, i.e., oxygen does not form long-lived surface functional groups during oxidation. The results from LII and XPS thus demonstrate a decrease in fine-structure order with oxidation, but they show that oxidation has a much larger impact on the surface order than on the bulk. These results indicate that oxidation occurs predominantly at the particle surface and that the chemical structure of the bulk located beneath the surface of the shrinking soot particle remains relatively intact. Previous work has suggested that, under some conditions, soot can oxidize internally rather than at the surface through a process by which oxygen percolates into the particle and reacts with the less stable primary-particle core (Vander Wal et al. 2007). Our study is consistent with a recent study that showed that mature soot tends to oxidize at the surface (Sediako et al. 2017).

Ouf et al. (2016) have demonstrated that a small amount of surface oxidation can occur on *ex situ* samples of soot, even under conditions where atmospheric exposure is limited. They have observed as much as 10 at% O for less mature soot and 4 at% O for more mature soot. It is thus possible that the oxygenated species observed at the surface of the particles are related to sampling. This possibility would tend to strengthen our conclusions that oxidation occurs at the surface and leads to a loss of surface-maturity level that does not strongly influence the level of maturity of the core particle and that a significant amount of oxygen is not incorporated into the particle during oxidation. In addition, Ouf et al. (2016) found that oxidation of *ex situ* samples produces predominantly carbonyl (—C=O) and carboxyl (—COO/—COOH) functional groups. Our XPS fitting suggests that, below an HAB of ~6.5 mm, the majority of the oxygen bound to the particle surface is in the form of hydroxyl (—C—OH) and ether (—C—O—C—) groups. Above this HAB, i.e., where particle oxidation

occurs in the flame, the signal from hydroxyl and ether groups decreases sharply, and the small remaining oxygen signal stems from carbonyl and carboxyl functional groups.

These results indicate that the bulk and the surface of the soot particles may exhibit different levels of maturity. The surface- and bulk-maturity levels may evolve nearly independently under some conditions, and a soot particle can simultaneously undergo surface growth while the bulk-maturity level increases. Prior to oxidation, there is most likely a direct link between soot-maturity level and hydrogen content, but the connections become more complex during oxidation.

5. Summary and conclusions

This article presents results obtained using laser-induced incandescence (LII) and X-ray photoelectron spectroscopy (XPS) in a partially premixed atmospheric ethylene-air diffusion flame. We recorded LII measurements using laser wavelengths of 1064 and 532 nm as a function of the laser fluence and used these measurements to derive the dispersion exponent (ξ) and trends in the absorption cross-section scaling factor (β). We used these optical parameters to infer trends in the maturity level of the bulk of the particle. We fit the XPS spectra to derive the sp^2/defect ratio, thereby inferring the surface-maturity level. We combined these results with aerosol mass spectrometry (AMS) measurements of heavy hydrocarbon abundance to gain insight into surface-growth mechanisms.

Figure 4 schematically summarizes our results. At low HABs (2–3.5 mm), the particles are disordered and immature enough that they do not produce measureable LII signal and have very low sp^2/defect ratios. At HABs in the range of 3.5–5 mm, there is a dramatic increase in the LII signal and β accompanied by a decrease in ξ, demonstrating a sharp increase in the bulk-soot-maturity level with HAB in this region. The sp^2/defect ratio, an indicator of surface-maturity level, increases gradually with HAB in this region, which is also characterized by a high abundance of PAH and other heavy hydrocarbons, as measured by the AMS. We hypothesize that the adsorption of hydrogen-rich heavy hydrocarbons onto the particle surface at HABs below ~6 mm leads to particle growth, which prevents the surface from attaining the same maturity level as the bulk material. Under these conditions, the surface might not fully mature unless the concentrations of gas-phase PAHs and other hydrocarbon species are low. Where the heavy hydrocarbon abundance declines to nearly immeasurably small values, i.e., at HABs between 5 and ~6 mm, the surface-maturity level increases substantially and reaches a maximum

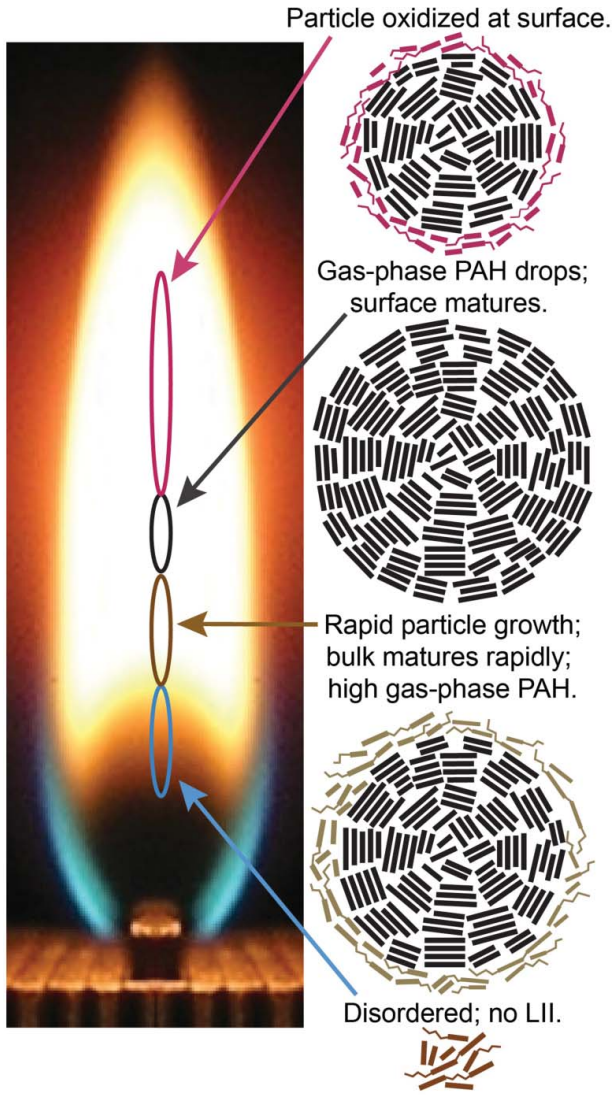

Figure 4. Summary of the changes in surface and bulk maturity during particle formation, growth, and oxidation. The photo shows the flame from the end, looking down the long-axis. Squiggly lines denote aliphatic groups, and thicker straight lines represent ring structures shown from the side. Ovals represent locations in the flame where the corresponding particle characteristics are observed. HABs are shown relative to the top of the fuel tubes (left axis). The oxidized and immature surfaces are shown as a layer of aromatic rings with aliphatic groups attached. Online color: The oxidized surface is highlighted in red; the immature surface during particle growth is shown in light brown. Mature material is shown as black.

while the bulk-maturity level does not change. In the region where the particles start to oxidize, at HABs above 6 mm, the volume fraction and surface order decrease dramatically. Although the bulk-fine-structure order decreases, the change is small compared with the decrease in the surface order. This result indicates that, under these combustion conditions, oxidation occurs at the surface, where it disrupts the surface aromaticity. As

outer layers are removed from the particle, the inner core of the particle stays intact.

These results thus demonstrate the independent evolution of the maturity level of soot at the surface of the particle and in the bulk for the flame conditions studied here. More work is required, however, to establish trends in maturity level under different combustion conditions. There is also a need to develop techniques that provide a more quantitative assessment of the chemical characteristics of the particles as they mature.

Acknowledgments

The authors dedicate this article to the memory of Prof. Mildred Dresselhaus who shaped the field of carbon science and inspired generations of scientists with her brilliance and dedication. The authors thank Loren Stacks and Daniel Strong for generating the illustrations in Figures S1 and S3.

Funding

This work was funded by the U.S. Department of Energy (DOE), Office of Basic Energy Sciences (BES). KOJ was supported by the Single Investigator Small Group Research (SISGR), Grant no. DE-SC0002619. MFC, PES, HAM, and experimental expenses were funded under DOE BES, the Division of Chemical Sciences, Geosciences, and Biosciences. Sandia National Laboratories is a multi-mission laboratory managed and operated by National Technology and Engineering Solutions of Sandia, LLC, a wholly owned subsidiary of Honeywell International, Inc., for the DOE's National Nuclear Security Administration under Contract no. DE-NA0003525.

References

Bambha, R. P., Dansson, M. A., Schrader, P. E., and Michelsen, H. A. (2013). Effects of Volatile Coatings on the Laser-Induced Incandescence of Soot. *Appl. Phys. B*, 112:343–358.

Batten, C. E. (1985). Spectral Optical Constants of Soots from Polarized Angular Reflectance Measurements. *Appl. Opt.*, 24:1193–1199.

Bejaoui, S., Lemaire, R., Desgroux, P., and Therssen, E. (2014). Experimental Study of the E (m, λ)/E (m, 1064) Ratio as a Function of Wavelength, Fuel Type, Height Above the Burner and Temperature. *Appl. Phys. B*, 116:313–323.

Bescond, A., Yon, J., Ouf, F.-X., Rozé, C., Coppalle, A., Parent, P., Ferry, D., and Laffon, C. (2016). Soot Optical Properties Determined by Analyzing Extinction Spectra in the Visible Near-UV: Toward an Optical Speciation According to Constituents and Structure. *J. Aerosol Sci.*, 101:118–132.

Bladh, H., Olofsson, N.-E., Mouton, T., Simonsson, J., Mercier, X., Faccinetto, A., Bengtsson, P.-E., and Desgroux, P. (2015). Probing the Smallest Soot Particles in Low-Sooting Premixed Flames Using Laser-Induced Incandescence. *Proc. Combust. Inst.*, 35:1843–1850.

Cain, J. P., Gassman, P. L., Wang, H., and Laskin, A. (2010). Micro-FTIR Study of Soot Chemical Composition—Evidence of Aliphatic Hydrocarbons on Nascent Soot Surfaces. *Phys. Chem. Chem. Phys.*, 12:5206–5218.

Campbell, M., Bohlin, G., Schrader, P., Bambha, R., Kliewer, C., Johansson, K., and Michelsen, H. (2016). Design and Characterization of a Linear Hencken-Type Burner. *Rev. Sci. Instrum.*, 87:115114.

Cléon, G., Amodeo, T., Faccinetto, A., and Desgroux, P. (2011). Laser Induced Incandescence Determination of the Ratio of the Soot Absorption Functions at 532 nm and 1064 nm in the Nucleation Zone of a Low Pressure Premixed Sooting Flame. *Appl. Phys. B*, 104:297–305.

D'Alessio, A., Beretta, F., and Venitozzi, C. (1972). Optical Investigations of Soot Forming Methane-Oxygen Flames. *Combust. Sci. Technol.*, 5:263–272.

Dalzell, W. H., and Sarofim, A. F. (1969). Optical Constants of Soot and Their Application to Heat-Flux Calculations. *J. Heat Transfer*, 91:100–104.

di Stasio, S., Mitchell, J. B. A., LeGarrec, J. L., Biennier, L., and Wulff, M. (2006). Synchrotron SAXS in Situ Identification of Three Different Size Modes for Soot Nanoparticles in a Diffusion Flame. *Carbon*, 44:1267–1279.

DOE. (2006). *Report of the Basic Energy Sciences Workshop on Basic Research Needs for Clean and Efficient Combustion of 21st Century Transportation Fuels*, Office of Science, U.S. Department of Energy, Germantown, MD.

Foster, P. J., and Howarth, C. R. (1968). Optical Constants of Carbons and Coals in the Infrared. *Carbon*, 6:719–729.

Goulay, F., Schrader, P. E., López-Yglesias, X., and Michelsen, H. A. (2013). A Dataset for Validation of Models of Laser-Induced Incandescence from Soot: Temporal Profiles of LII Signal and Particle Temperature. *Appl. Phys. B*, 112:287–306.

Goulay, F., Schrader, P. E., and Michelsen, H. A. (2009). The Effects of Pulsed Laser Injection Seeding and Triggering on the Temporal Behavior and Magnitude of Laser-Induced Incandescence of Soot. *Appl. Phys. B*, 96:613–621.

Grotheer, H.-H., Wolf, K., and Hoffmann, K. (2011). Photoionization Mass Spectrometry for the Investigation Of combustion Generated Nascent Nanoparticles and Their Relation To laser Induced Incandescence. *Appl. Phys. B*, 104:367–383.

Habib, Z. G., and Vervisch, P. (1988). On the Refractive Index of Soot at Flame Temperature. *Combust. Sci. Technol.*, 59:261–274.

Hopkins, R. J., Lewis, K., Desyaterik, Y., Wang, Z., Tivanski, A. V., Arnott, W. P., Laskin, A., and Gilles, M. K. (2007). Correlations Between Optical, Chemical, and Physical Properties of Biomass Burn Aerosols. *Geophys. Res. Lett.*, 34: L18806.

Jaramillo, I. C., Gaddam, C. K., Vander Wal, R. L., Huang, C.-H., Levinthal, J. D., and Lighty, J. S. (2014). Soot Oxidation Kinetics Under Pressurized Conditions. *Combust. Flame*, 161:2951–2965.

Johansson, K. O., Dillstrom, T., Monti, M., El Gabaly, F., Campbell, M. F., Schrader, P. E., Popolan-Vaida, D. M., Richards-Henderson, N. K., Wilson, K. R., and Violi, A. (2016). Formation and Emission of Large Furans and Oxygenated Hydrocarbons from Flames. *Proc. Natl. Acad. Sci. U.S.A.*, 113:8374–8379.

Kim, J., Bauer, H., Dobovicnik, T., Hitzenberger, R., Lottin, D., Ferry, D., and Petzold, A. (2015). Assessing Optical Proper-

ties and Refractive Index of Combustion Aerosol Particles Through Combined Experimental and Modeling Studies. *Aerosol Sci. Technol.*, 49:340–350.

Leschowski, M., Thomson, K., Snelling, D., Schulz, C., and Smallwood, G. (2015). Combination of LII and Extinction Measurements for Determination of Soot Volume Fraction and Estimation of Soot Maturity in Non-Premixed Laminar Flames. *Appl. Phys. B*, 119:685–696.

López-Yglesias, X., Schrader, P. E., and Michelsen, H. A. (2014). Soot Maturity and Absorption Cross Sections. *J. Aerosol Sci.*, 75:43–64.

McKinnon, J. T., Meyer, E., and Howard, J. B. (1996). Infrared Analysis of Flame Generated PAH Samples. *Combust. Flame*, 105:161–166.

Michelsen, H. (2017). Probing Soot Formation, Chemical and Physical Evolution, and Oxidation: A Review of *in situ* Diagnostic Techniques and Needs. *Proc. Combust. Inst.*, 36:717–735.

Michelsen, H., Schulz, C., Smallwood, G., and Will, S. (2015). Laser-Induced Incandescence: Particulate Diagnostics for Combustion, Atmospheric, and Industrial Applications. *Prog. Energy Combust. Sci.*, 51:2–48.

Michelsen, H. A. (2003). Understanding and Predicting the Temporal Response of Laser-Induced Incandescence from Carbonaceous Particles. *J. Chem. Phys.*, 118:7012–7045.

Michelsen, H. A., Schrader, P. E., and Goulay, F. (2010). Wavelength and Temperature Dependences of the Absorption and Scattering Cross Sections of Soot. *Carbon*, 48:2175–2191.

Michelsen, H. A., Schrader, P. E., and Goulay, F. (2012). Erratum to "Wavelength and Temperature Dependences of the Absorption and Scattering Cross Sections of Soot" [Carbon 48 (2010) 2175–2191]. *Carbon*, 50:740.

Migliorini, F., De Iuliis, S., Maffi, S., and Zizak, G. (2015). Saturation Curves of Two-Color Laser-Induced Incandescence Measurements for the Investigation of Soot Optical Properties. *Appl. Phys. B*, 120:417–427.

Migliorini, F., Thomson, K., and Smallwood, G. (2011). Investigation of Optical Properties of Aging Soot. *Appl. Phys. B*, 104:273–283.

Millikan, R. C. (1961). Optical Properties of Soot. *J. Opt. Soc. America*, 51:698–699.

Minutolo, P., Gambi, G., and D'alessio, A. (1996). The Optical Band Gap Model in the Interpretation of the UV-Visible Absorption Spectra of Rich Premixed Flames, in *Symposium (International) on Combustion*, Elsevier, pp. 951–957.

Mouton, T., Mercier, X., Wartel, M., Lamoureux, N., and Desgroux, P. (2013). Laser-Induced Incandescence Technique to Identify Soot Nucleation and Very Small Particles in Low-Pressure Methane Flames. *Appl. Phys. B*, 112:369–379.

Müller, J.-O., Su, D. S., Wild, U., and Schlögl, R. (2007). Bulk and Surface Structural Investigations of Diesel Engine Soot and Carbon Black. *Phys. Chem. Chem. Phys.*, 9:4018–4025.

Öktem, B., Tolocka, M. P., Zhao, B., Wang, H., and Johnston, M. V. (2005). Chemical Species Associated with the Early Stage of Soot Growth in a Laminar Premixed Ethylene–Oxygen–Argon Flame. *Combust. Flame*, 142:364–373.

Olofsson, N.-E., Simonsson, J., Török, S., Bladh, H., and Bengtsson, P.-E. (2015). Evolution of Properties of Aging Soot in Premixed Flat Flames Studied by Laser-Induced Incandescence and Elastic Light Scattering. *Appl. Phys. B*, 119:669–683.

Ouf, F.-X., Parent, P., Laffon, C., Marhaba, I., Ferry, D., Marcillaud, B., Antonsson, E., Benkoula, S., Liu, X.-J., Nicolas, C., Robert, E., Patanen, M., Barreda, F.-A., Sublemontier, O., Coppalle, A., Yon, J., Miserque, F., Mostefaoui, T. A., Regier, T. Z., Mitchell, J. B. A., and Miron, C. (2016). First in-Flight Synchrotron X-Ray Absorption and Photoemission Study of Carbon Soot Nanoparticles. *Sci. Rep.*, 6:36495.

Pokhrel, R. P., Wagner, N. L., Langridge, J. M., Lack, D. A., Jayarathne, T., Stone, E. A., Stockwell, C. E., Yokelson, R. J., and Murphy, S. M. (2016). Parameterization of Single-Scattering Albedo (SSA) and Absorption Ångström Exponent (AAE) with EC/OC for Aerosol Emissions from Biomass Burning. *Atmos. Chem. Phys.*, 16:9549–9561.

Richter, H., and Howard, J. B. (2000). Formation of Polycyclic Aromatic Hydrocarbons and Their Growth to Soot—A Review of Chemical Reaction Pathways. *Prog. Energy Combust. Sci.*, 26:565–608.

Russo, C., Tregrossi, A., and Ciajolo, A. (2015). Dehydrogenation and Growth of Soot in Premixed Flames. *Proc. Combust. Inst.*, 35:1803–1809.

Santamaria, A., Mondragón, F., Molina, A., Marsh, N. D., Eddings, E. G., and Sarofim, A. F. (2006). FT-IR and 1H NMR Characterization of the Products of an Ethylene Inverse Diffusion Flame. *Combust. Flame*, 146:52–62.

Santamaria, A., Yang, N., Eddings, E., and Mondragon, F. (2010). Chemical and Morphological Characterization of Soot and Soot Precursors Generated in an Inverse Diffusion Flame with Aromatic and Aliphatic Fuels. *Combust. Flame*, 157:33–42.

Schnaiter, M., Gimmler, M., Llamas, I., Linke, C., Jäger, C., and Mutschke, H. (2006). Strong Spectral Dependence of Light Absorption by Organic Carbon Particles Formed by Propane Combustion. *Atmos. Chem. Phys.*, 6:2981–2990.

Sediako, A. D., Soong, C., Howe, J. Y., Kholghy, M. R., and Thomson, M. J. (2017). Real-time observation of soot aggregate oxidation in an Environmental Transmission Electron Microscope. *Proc. Combust. Inst.*, 36:841–851.

Siddall, R. G., and McGrath, I. A. (1963). The Emissivity of Luminous Flames. *Proc. Combust. Inst.*, 9:102–110.

Simonsson, J., Olofsson, N.-E., Török, S., Bengtsson, P.-E., and Bladh, H. (2015). Wavelength Dependence of Extinction in Sooting Flat Premixed Flames in the Visible and Near-Infrared Regimes. *Appl. Phys. B*, 119:657–667.

Smith, M., Scudiero, L., Espinal, J., McEwen, J.-S., and Garcia-Perez, M. (2016). Improving the Deconvolution and Interpretation of XPS Spectra from Chars by ab initio Calculations. *Carbon* 110:155–171.

Spence, G. B. (1963). *Research and Development of Advanced Graphite Materials. Volume 41: Survey and Analytical Representation of the Measurements of the Specific Heat of Graphite*. Technical Report No WADD-TR-61-72. Defense Documentation Center, Alexandria, VA.

Su, Y., Sipin, M. F., Prather, K. A., Gelein, R. M., Lunts, A., and Oberdorster, G. (2005). ATOFMS Characterization of Individual Model Aerosol Particles Used for Exposure Studies. *Aerosol Sci. Technol.*, 39:400–407.

Tanuma, S., Powell, C. J., and Penn, D. R. (2011). Calculations of Electron Inelastic Mean Free Paths. IX. Data for 41 Elemental Solids Over the 50 eV to 30 keV Range. *Surf. Interface Anal.*, 43:689–713.

Therssen, E., Bouvier, Y., Schoemaecker-Moreau, C., Mercier, X., Desgroux, P., Ziskind, M., and Focsa, C. (2007). Determination of the Ratio of Soot Refractive Index Function E (m) at the Two Wavelengths 532 and 1064 nm by Laser Induced Incandescence. *Appl. Phys. B*, 89:417–427.

Vander Wal, R. L., Yezerets, A., Currier, N. W., Kim, D. H., and Wang, C. M. (2007). HRTEM Study of Diesel Soot Collected from Diesel Particulate Filters. *Carbon*, 45:70–77.

Wang, H. (2011). Formation of Nascent Soot and Other Condensed-Phase Materials in Flames. *Proc. Combust. Inst.*, 33:41–67.

Wentzel, M., Gorzawski, H., Naumann, K.-H., Saathoff, H., and Weinbruch, S. (2003). Transmission Electron Microscopical and Aerosol Dynamical Characterization of Soot Aerosols. *J. Aerosol Sci.*, 34:1347–1370.

Yapp, E. K. Y., Patterson, R. I. A., Akroyd, J., Mosbach, S., Adkins, E. M., Miller, J. H., and Kraft, M. (2016). Numerical Simulation and Parametric Sensitivity Study of Optical Band Gap in a Laminar Co-Flow Ethylene Diffusion Flame. *Combust. Flame*, 167:320–334.

Yon, J., Lemaire, R., Therssen, E., Desgroux, P., Coppalle, A., and Ren, K. (2011). Examination of Wavelength Dependent Soot Optical Properties of Diesel and Diesel/Rapeseed Methyl Ester Mixture by Extinction Spectra Analysis and LII Measurements. *Appl. Phys. B*, 104:253–271.